Dc Liquid Metal Magnetohydrodynamic Power Generation

Author(s): David G. Elliott

Session Name: All

SEAM: 6 (1965)

SEAM EDX URL: https://edx.netl.doe.gov/dataset/seam-6

EDX Paper ID: 142

DC LIQUID-METAL MAGNETOHYDRODYNAMIC POWER GENERATION*

David G. Elliott

Supervisor, Energy Conversion Group
Jet Propulsion Laboratory
Pasadena, California

Abstract

A constant-pressure DC magnetohydrodynamic generator was tested with NaK at inlet velocities up to 300 ft/sec. The maximum output power was 10.8 kw (18,250 amp at 0.59 v) and the efficiency was 48%. The theoretical efficiency, considering ohmic heating, fluid friction, boundary layer shunting, and end effects, was 58%. The theoretical ultimate efficiency of liquid-metal MHD generators, of the type considered, ranges from 60 to 70%.

Introduction

The possible availability of cycles for accelerating liquid metals and circulating them, with net available power, in a closed loop[1] has spurred interest in liquid-metal MHD generators. The required operating conditions of such generators are: liquid inlet velocity = 300-600 ft/sec, exit velocity = 50-80% of inlet velocity, pressure drop ≅ 0, flow rate = 0.5-2.0 lb/sec per kw, and liquid temperature = 1000-2000°F.

To investigate the feasibility of DC liquid-metal generators, an experimental 10-kw generator was tested with cold NaK (78% potassium, 22% sodium) at inlet velocities up to 300 ft/sec, and the results were compared with the most complete available theory.

Theoretical Performance

Idealized Generator

The experimental generator was designed to match as closely as possible the idealized configuration shown in Fig. 1. The idealized generator consists of a diverging rectangular duct of inlet width a_1 between the electrode faces, exit width a_2, height b between the magnet faces, and length L. The magnet faces of the channel, as well as the inlet and outlet ducts, are insulated from the liquid metal.

A magnetic field B is applied in the b-direction. The field has a constant value B_0 over the length L and decreases exponentially with an e-folding length x_{e_1} upstream and x_{e_2} downstream.

Liquid metal of density ρ, viscosity μ_f, and electrical conductivity σ flows through the generator from pressure $p_{-\infty}$ to pressure p_{∞} at volume flow rate $\dot{v}$ and mass flow rate $\dot{m}$. The pressures at the inlet and exit of the diverging section are p_1 and p_2, respectively. The velocity u of the liquid at distance x from the generator inlet is a function of the distance z from the electrode face and the distance y from the magnet face. The center line velocity is u_0.

A voltage difference E is maintained between the liquid-metal interfaces in contact with the electrodes, and current I_L and power $P_e = EI_L$ are delivered to the load. The power extracted from the liquid, through velocity change and pressure drop, is P_m.

Assumptions

1. The flow is turbulent and fully developed with a 1/7-power velocity profile.

2. The wall shear is unaffected by magnetohydrodynamic effects.

3. The divergence angle of the generator is small enough that the velocity can be considered parallel to the axis and perpendicular to the current.

4. Current compensation is provided by backstraps such that the field in the liquid is equal to the applied field.

5. The fluid properties are constant.

Assumption 1 is valid at the high Reynolds numbers of interest (10^5 - 10^7). Available information[2] indicates that Assumption 2 should also be valid at these Reynolds numbers. Assumption 3 was closely met by the experimental generator which had a total divergence angle of 3.7 deg. Assumption 4 was met as closely as possible in the experimental generator by providing heavy backstraps, but compensation by this method is only approximate because of the axial variation of current density and the presence of shunt end currents. Assumption 5 is valid because of the liquid incompressibility (the generator is presumed to be thermally insulated so that temperature change is negligible).

Input Power Definition

To determine the fluid input power, it is necessary to define where the generator begins and ends with respect to fluid friction. In the applications of interest[1], the inlet and outlet ducting can be considered portions of the adjoining components and the friction losses can be assigned to the latter. Hence, the input power will be defined to be the power extracted between $p_{-\infty}$ and p_{∞} with frictionless flow in the inlet and outlet ducts.

Analysis

Consider an element of liquid of length a and cross section dxdy located distance y from the magnet face and distance x from the generator inlet. The resistance of this element to current flow between the electrodes is

$$R = \frac{a}{\sigma\, dxdy} \tag{1}$$

By Assumptions 3 and 4 the voltage induced between the ends of the element is

*This paper presents the results of one phase of research carried out at the Jet Propulsion Laboratory, California Institute of Technology, under Contract No. NAS 7-100, sponsored by the National Aeronautics and Space Administration.

$$E_i(x, y) = B_0 \int_0^a u\, dz \tag{2}$$

The current through the element is

$$dI(x, y) = \frac{E_i - E}{R}$$

$$= \frac{\sigma}{a}(E_i - E)\, dxdy \tag{3}$$

and the ohmic heating loss is

$$dP_r(x, y) = \frac{\left(E_i - E\right)^2}{R}$$

$$= \frac{\sigma}{a}\left(E_i - E\right)^2 dxdy \tag{4}$$

The current through the entire sheet of liquid of length dx at station x is

$$dI(x) = \frac{\sigma\, dx}{a} \int_0^b (E_i - E)\, dy \tag{5}$$

and the ohmic heating loss is

$$dP_r(x) = \frac{\sigma\, dx}{a} \int_0^b \left(E_i - E\right)^2 dy \tag{6}$$

Substituting E_i from Eq. 2, the current in the incremental sheet is

$$dI(x) = \frac{\sigma\, dx}{a}\left[B_0 \int_0^b \int_0^a u\, dzdy - E \int_0^b dy\right] \tag{7}$$

and the ohmic heating is

$$dP_r(x) = \frac{\sigma\, dx}{a}\left[B_0^2 \int_0^b \left(\int_0^a u\, dz\right)^2 dy\right.$$

$$\left. - 2EB_0 \int_0^b \int_0^a u\, dzdy + E^2 \int_0^b dy\right] \tag{8}$$

The double integral in the above equations is exactly the volume flow rate, $\dot{v}$. In terms of the bulk velocity V,

$$Vab = V_1 a_1 b = \dot{v} = \int_0^b \int_0^a u\, dzdy \tag{9}$$

Substituting Eq. 9 into Eq. 7,

$$dI(x) = \sigma B_0 V_1 a_1 b(1 - \mu) \frac{dx}{a} \tag{10}$$

where μ is the loading ratio defined by

$$\mu = \frac{E}{B_0 V_1 a_1} \tag{11}$$

By Assumption 1, the velocity distribution in the y-direction is

$$\frac{u}{u_0} = \left(\frac{y}{b/2}\right)^{1/7} \tag{12}$$

Using this relation to evaluate the first term in Eq. 8, with the approximation

$$\int_0^a u\, dz \cong ua$$

the result is

$$\int_0^b \left(\int_0^a u\, dz\right)^2 dy = \frac{7}{9} u_0^2 a^2 b \tag{13}$$

For the same profile, Eq. 9 gives

$$V = \frac{7}{8} u_0 \tag{14}$$

Substituting Eqs. 9, 13, and 14 into Eq. 8, the ohmic heating is

$$dP_r(x) = \sigma B_0^2 V_1^2 a_1^2 b(1 - \mu)^2 \left[1 + \frac{1}{63(1 - \mu)^2}\right] \frac{dx}{a} \tag{15}$$

The power dissipated in friction within the element dx is the product of the velocity and the retarding force due to wall shear. Thus,

$$dP_f(x) = \frac{\rho V^3 C_f}{2}\left[2(a + b)\, dx\right]$$

$$= \rho C_f V_1^3 a_1^3 \left(\frac{a + b}{a^3}\right) dx \tag{16}$$

where C_f is the skin-friction coefficient (one quarter of the friction factor f). C_f is nearly constant over the length of the channel and can, therefore, be evaluated at the mean Reynolds number

$$Re = \frac{\dot{m} D_h}{a_m b \mu_f} \tag{17}$$

where D_h is the mean hydraulic diameter

$$D_h = \frac{2a_m b}{a_m + b} \tag{18}$$

C_f can be calculated from the Prandtl relation[3]

$$\frac{1}{\sqrt{C_f}} = 4 \log_{10}\left(2\, Re \sqrt{C_f}\right) - 0.8 \tag{19}$$

Integrating Eqs. 10, 15, and 16 between x = 0 and L, the total current, ohmic heating, and friction power within the diverging channel are, respectively,

$$I = \frac{\sigma B_0 V_1 a_1 b L(1 - \mu)}{a_m} \tag{20}$$

$$P_r = \frac{\sigma B_0^2 V_1^2 a_1^2 bL(1-\mu)^2}{a_m}\left[1 + \frac{1}{63(1-\mu)^2}\right] \quad (21)$$

$$P_f = \frac{\rho C_f V_1^3 a_1^2 L}{a_2}\left[1 + \frac{b}{2}\left(\frac{1}{a_1} + \frac{1}{a_2}\right)\right] \quad (22)$$

where a_m is the mean width defined by

$$\frac{L}{a_m} = \int_0^L \frac{dx}{a} \quad (23)$$

For a linearly tapered channel

$$a_m = a_1 \frac{\frac{a_2}{a_1} - 1}{\ln \frac{a_2}{a_1}} \quad (24)$$

The power output to the electrodes is

$$P_{e_0} = EI$$

$$= \frac{\sigma B_0^2 V_1^2 a_1^2 bL\mu(1-\mu)}{a_m} \quad (25)$$

This is identical to the one-dimensional slug-flow relation. The only effect of the boundary layer on the electrical performance of the generator is the added ohmic heating given by the term $1/63(1-\mu)^2$ in Eq. 21; at a typical loading of $\mu = 0.8$ the increase in ohmic heating is 40%, resulting in a power output decrease of about 8%.

The total fluid input power to the divergent channel is

$$P_{m_0} = P_{e_0} + P_r + P_f$$

$$= \frac{\sigma B_0^2 V_1^2 a_1^2 bL(1-\mu)}{a_m}\left[1 + \frac{1}{1-\mu} \times \left\{\frac{1}{63} + \frac{\rho C_f V_1 a_m}{\sigma B_0^2 a_2 b}\left[1 + \frac{b}{2}\left(\frac{1}{a_1} + \frac{1}{a_2}\right)\right]\right\}\right] \quad (26)$$

The source of this fluid input power is the change of fluid kinetic power due to velocity decrease, plus the $\dot{v}\Delta p$ power resulting from any pressure change $\Delta p = p_1 - p_2$. The kinetic power in the flow at any station x is

$$P_k = \int_0^b \int_0^a \frac{\rho u^3}{2} dz dy \quad (27)$$

For the velocity profile of Eq. 12, with the slit channel approximation

$$\int_0^a u^3 \, dz \cong u^3 a$$

this reduces to

$$P_k = \frac{128}{245}\rho V^3 ab = 1.045\left(\frac{\dot{m}V^2}{2}\right) \quad (28)$$

The factor 1.045 represents the increase in kinetic power over slug flow at the bulk velocity V. For a circular channel the factor is 1.058; thus, an uncertainty of only 1.3% in the kinetic power is introduced by ignoring the aspect ratio of the cross section.

Evaluating the kinetic power at each end from Eq. 28 and adding the $\dot{v}\Delta p$ power, the power input to the diverging channel is

$$P_{m_0} = \frac{128}{245}\rho V_1^3 a_1 b\left[1 - \left(\frac{a_1}{a_2}\right)^2\right] + V_1 a_1 b \Delta p \quad (29)$$

This must equal the power extracted by electrical and friction effects as given by Eq. 26. Equating these two expressions and solving for B_0, the field that must be applied is

$$B_0 = \left[\frac{\rho V_1 a_m}{\sigma bL\left(\frac{64}{63} - \mu\right)}\left\{\frac{128b}{245a_1}\left[1 - \left(\frac{a_1}{a_2}\right)^2\right] + \frac{b\Delta p}{\rho V_1^2 a_1} - \frac{C_f L}{a_2}\left[1 + \frac{b}{2}\left(\frac{1}{a_1} + \frac{1}{a_2}\right)\right]\right\}\right]^{1/2} \quad (30)$$

Only the current flowing across the diverging channel has been considered so far. There are, in addition, currents that flow through the fluid upstream and downstream of the diverging section. If the field falls steeply at the ends, or the loading ratio is high, the fluid at each end acts as a shunt resistor and draws current that would otherwise have gone to the load. If the field extends sufficiently far and the loading ratio is sufficiently low, the fluid at each end acts as a generator and adds to the output.

Sutton, Hurwitz, and Poritsky[4] show that these shunt end currents reduce (or, if the sign is negative, increase) the power output by*

$$\Delta P_e = \frac{\sigma B_0^2 V_1^2 a_1^2 b\mu}{\pi}\left[2\mu \ln 2 - (\alpha_1 + \alpha_2)\right] \quad (31)$$

and increase the required fluid input power by**

*In Ref. 4, multiply Eq. 17 by Eq. 10 and by 1/2 to obtain the power loss at each end with zero field extension. Make the notation changes $\eta \rightarrow \mu$, unit height $\rightarrow$ b, h $\rightarrow$ a_1 or a_2, and add the loss at each end to obtain the first term in Eq. 31 above. Take 1/2 of Eq. 71 (correcting the misprinted $\pi^{-1/2}$ term to π^{-1}) to obtain the power gained back at each end due to field extension, change β_1 to α_1 or α_2, and add the power gain at each end to give the second term in Eq. 31 above. The α expressions are from Eq. 20 of Ref. 4. The relations apply for $L/a_m > 0.3$.

**In Ref. 4, multiply the first two terms in Eq. 91 (which represent pressure increases) by $-\dot{v}/2 = Ubh/2$ to obtain the added fluid power at each end due to field extension. Call the bracketed expression $-\beta$ (instead of β_3) and add the power at each end to obtain Eq. 32.

$$\Delta P_m = \frac{\sigma B_0^2 V_1^2 a_1^2 b\mu}{\pi}\left[\frac{\pi(\beta_1 + \beta_2)}{2\mu} - (\alpha_1 + \alpha_2)\right] \tag{32}$$

where

$$\alpha_1 = \frac{\pi x_{e_1}}{a_1}\left[1 - \frac{1}{\sqrt{\pi}}\frac{\Gamma\frac{1}{2}\left(\frac{a_1}{\pi x_{e_1}} + 1\right)}{\Gamma\frac{1}{2}\left(\frac{a_1}{\pi x_{e_1}} + 2\right)}\right] \tag{33}$$

and

$$\alpha_2 = \frac{\pi x_{e_2}}{a_2}\left[1 - \frac{1}{\sqrt{\pi}}\frac{\Gamma\frac{1}{2}\left(\frac{a_2}{\pi x_{e_2}} + 1\right)}{\Gamma\frac{1}{2}\left(\frac{a_2}{\pi x_{e_2}} + 2\right)}\right] \tag{34}$$

The quantities β_1 and β_2 are functions of y_e, which is given by

$$y_{e_1} = \frac{2\pi x_{e_1}}{a_1} \tag{35}$$

$$y_{e_2} = \frac{2\pi x_{e_2}}{a_2} \tag{36}$$

The relationship between β and y_e is defined by Eq. 91 of Ref. 4 and plotted there in Fig. 18. The curve is reproduced here in Fig. 2.

From Eqs. 25 and 31, the net output power of the generator is

$$P_e = P_{e_0} - \Delta P_e$$

$$= \frac{\sigma B_0^2 V_1^2 a_1^2 bL\mu(1 - \mu)}{a_m} \times \left[1 - \frac{2a_m \mu \ln 2}{\pi L(1 - \mu)} + \frac{a_m(\alpha_1 + \alpha_2)}{\pi L(1 - \mu)}\right] \tag{37}$$

The first term in Eq. 37 gives the power delivered to the electrodes by the fluid in the diverging channel. The second term gives the power drawn by the fluid at the ends, and the third term gives the reduction, or reversal, of that power.

From Eqs. 26 and 32, with B_0 evaluated from Eq. 30, the total input power is shown in Eq. 38.

The first term in Eq. 38 gives the power input in the absence of boundary layer, friction loss, or end effects. The second term gives the additional power input required for the boundary-layer loss, the third term the power for the end losses, and the fourth term the power to overcome friction in the diverging channel (the friction in the inlet and outlet ducts being excluded, as discussed earlier).

Dividing Eq. 37 by 38, the efficiency of the generator is shown in Eq. 39.

$$P_m = P_{m_0} + \Delta P_m$$

$$= \frac{\sigma B_0^2 V_1^2 a_1^2 bL(1 - \mu)}{a_m}\left[1 + \frac{1}{1 - \mu}\left\{\frac{1}{63} + \frac{a_m}{L}\left[\frac{\beta_1 + \beta_2}{2} - \frac{\mu(\alpha_1 + \alpha_2)}{\pi}\right] + \frac{\left(\frac{64}{63} - \mu\right)\left[1 + \frac{b}{2}\left(\frac{1}{a_1} + \frac{1}{a_2}\right)\right]}{\frac{128b}{245}\left(\frac{1}{a_1} + \frac{1}{a_2}\right)\left(\frac{a_2 - a_1}{LC_f} - \frac{245}{256}\right) + \frac{a_2 b\Delta p}{\rho V_1^2 a_1 LC_f} - 1}\right\}\right] \tag{38}$$

$$\eta = \mu \frac{1 - \frac{2a_m \mu \ln 2}{\pi L(1 - \mu)}\left(1 - \frac{\alpha_1 + \alpha_2}{2\mu \ln 2}\right)}{1 + \frac{1}{1 - \mu}\left\{\frac{1}{63} + \frac{a_m}{L}\left[\frac{\beta_1 + \beta_2}{2} - \frac{\mu(\alpha_1 + \alpha_2)}{\pi}\right] + \frac{\left(\frac{64}{63} - \mu\right)\left[1 + \frac{b}{2}\left(\frac{1}{a_1} + \frac{1}{a_2}\right)\right]}{\frac{128b}{245}\left(\frac{1}{a_1} + \frac{1}{a_2}\right)\left(\frac{a_2 - a_1}{LC_f} - \frac{245}{256}\right) + \frac{a_2 b\Delta p}{\rho V_1^2 a_1 LC_f} - 1}\right\}} \tag{39}$$

Figure 3 illustrates the type of behavior predicted by the theory, with and without boundary layer and field extension, for the geometry of the experimental generator at the C_f corresponding to the highest inlet velocity attained (301 ft/sec). The efficiency is zero at $\mu = 0$ (short circuit), rises to a peak, and falls to zero again when the electrode voltage is just far enough below the induced voltage to furnish the shunt end currents.

The theoretical efficiency with both the 1/7-power boundary-layer profile and an exponential field extension of e-folding length $x_{e1} = x_{e2} =$ 0.89 in., as calculated from Eq. 39, is given by the middle curve; the peak value is $\eta = 0.60$ at $\mu = 0.86$. The efficiency in the absence of a boundary layer (slug flow), as calculated from Eq. 39 with $1/63 \rightarrow 0$, $64/63 \rightarrow 1$, $128/245 \rightarrow 1/2$, and $245/256 \rightarrow 1$, is given by the upper curve; the peak efficiency is raised to 0.66. The efficiency in the absence of a field extension, in addition, as obtained by also eliminating the α and β terms in Eq. 39, is given by the lower curve, which reaches only 0.51.

The measured efficiency of 0.48 for the 301-ft/sec run discussed later is also shown for comparison.

It is seen that an exponential field extension is highly beneficial and that the boundary-layer loss is not a major one. Eq. 39, incorporating both effects, represents the most complete theory available and will be used in the comparisons with the experimental data.

Experimental Generator

Figure 4 is a photograph of the experimental generator. The center portion, carrying the diverging channel, was made from a single copper block by cutting a deep slot to form one electrode and the magnet walls. The latter, with added external copper bars, also served as the backstraps. The other electrode was a tongue that fitted into the slot and was fastened by insulated bolts and sealed by an O-ring. The inlet and outlet ducts were attached to the copper block by insulated bolts and sealed by O-rings. All internal and mating surfaces of the copper block, except the electrode face, had a polyurethane coating of about 0.002-in. thickness to insulate the electrodes from each other, the magnet faces from the NaK, and the copper block from the ground potential of the piping. The inlet and outlet ducts, inlet nozzle, and piping were coated internally to prevent shunt currents other than through the NaK.

Figure 5 shows the geometry of the flow channel. The NaK was fed at high pressure to the inlet nozzle and accelerated to velocity V_1 in the inlet duct of dimensions $a_1 = 0.578$ in. and $b = 0.248$ in. After traversing the 2.7-in. inlet duct, the NaK decelerated in the constant-height diverging channel of length $L = 5.85$ in. to an exit width of $a_2 = 0.958$ in. The NaK then flowed through the 2.7-in. exit duct and returned to low velocity in the exit pipe.

Pressure taps of 0.04-in. diameter were located at the positions shown. The $p_{-\infty}$ and p_{∞} taps were presumed to read the pressures beyond the range of electrical effects, and the p_1 and p_2 taps represented the diverging channel inlet and outlet pressures, respectively.

Magnet and NaK Supply System

Figure 6 is a photograph of the generator mounted between the poles of the 6-in. laboratory magnet employed, and connected to the NaK supply system and to water-cooled load resistors.

The rectangular magnet poles were 5.8 in. long and 2.0 in. wide, with the ends cusped to flatten the field. The field was uniform within ±2% over most of the diverging channel but dropped 10% at the ends. The variation along the generator axis for a center field of 6 kilogauss is shown in Fig. 7 and compared with a constant value over the diverging channel plus an exponential extension of 0.89-in. e-folding length. The latter distribution was employed in the theoretical calculations.

The NaK entered the test cell from a 250-gal tank in an adjoining cubicle, flowed through a turbine flow meter, through a pneumatic valve (foreground, Fig. 6) for starting and stopping the flow, into the generator, through a remotely operated throttling valve for back-pressure control, and back to a receiver tank in the adjoining cubicle. Feed pressures of up to 1000 psig were obtained by pressurizing the supply tank with nitrogen. About 1000 lb of NaK could be transferred in one or more runs, after which the supply tank was vented and the receiver tank pressurized to return the NaK.

Instrumentation

The NaK flow rate was metered by the turbine meter, previously calibrated with water. The NaK flow data had an estimated accuracy of ±0.7%. Pressures in the generator and in the inlet and outlet ducts were measured with strain-gage transducers with an accuracy of ±0.5%. A differential pressure transducer was employed between p_1 and p_2.

The generator output current was determined from the voltage across the load resistors, which consisted of four water-cooled 3/8-in. -OD copper tubes in parallel. The resistance of the tubes, accurately determined at 68°F, was corrected to the run temperatures (86°F maximum), which were measured with thermocouples.

The generator output voltage at the electrode faces was determined from probes imbedded in the electrodes. The face potential of the tongue electrode was extrapolated from measurements at the flange and center, a correction of about 2.5%. The voltage and current measurements were estimated to be accurate within ±0.5%.

The applied magnetic field was determined from the magnet current and a prior calibration with a Hall-effect probe. The accuracy was about ±2%.

NaK Properties

The NaK properties required in the evaluation of the data and in the theoretical calculations were density ρ, electrical resistivity $\mathcal{R} = 1/\sigma$, and viscosity μ_f. Only an approximate value of the latter was required since it entered only into the Reynolds number.

The density was measured at the 65°F run temperature by floating a glass hydrometer in a sample of the NaK under nitrogen in a Lucite cylinder. The value was $\rho = 0.878\ \text{g/cm}^3 = 54.76\ \text{lb/ft}^3 \pm 0.3\%$.

The electrical resistivity was determined by passing a known current through a 0.75-in.-ID x 36-in.-long Lucite tube filled with a sample of the NaK and measuring the voltage drop between probes 18 in. apart. The resistivity was $\mathscr{R} = 31.4\ \mu\text{ohm-cm} \pm 1\%$.

The viscosity value used was $\mu_f = 1.9$ lbm/ft hr, from Ref. 5.

Test Procedure

The NaK supply tank was pressurized to the value for the desired flow rate, and the magnet current was set to the value predicted to give zero pressure drop, $p_1 - p_2 = 0$, in the generator. The upstream valve was opened, establishing steady flow in about 5 sec. The generator pressure drop was then set as closely as possible to zero by adjusting the magnet current. After the desired conditions were reached the data were recorded and the run was terminated.

Test Operations

The results presented here were obtained in the third series of tests. The first series was with a straight-channel generator, results of which were reported in Ref. 6. The second series was with the divergent generator, but a failure of the insulation coating caused low performance. In the final series, six runs were made at successively increasing tank pressures up to 700 psig with satisfactorily steady flow conditions and near-zero pressure drop. On the attempted seventh run, at 800 psig tank pressure, the output voltage was low, indicating an insulation short. Upon disassembly, the generator was found to have a small burned spot in the insulation coating opposite one corner of the tongue electrode, possibly initiated by a pinhole short through the coating.

Experimental Performance

The electric power output was calculated as the product of the total current I_L through the load resistors and the electrode-face voltage E:

$$P_e = EI_L \tag{40}$$

The inlet velocity V_1 was calculated from the NaK volume flow rate and the inlet area using the definition

$$V_1 = \frac{\dot{v}}{a_1 b} \tag{41}$$

The loading ratio μ was calculated from V_1 and the applied field B_0 using the definition

$$\mu = \frac{E}{B_0 V_1 a_1} \tag{42}$$

The fluid power input to the diverging channel was calculated from the sum of the kinetic power change and $\dot{v}\Delta p$ power (see Eq. 29):

$$P_{m_0} = \frac{128}{245}\rho V_1^3 a_1 b\left[1 - \left(\frac{a_1}{a_2}\right)^2\right] + \dot{v}(p_1 - p_2) \tag{43}$$

The second term was a maximum of 2% of the first in the six runs.

The additional power inputs in the inlet and outlet ducts, in accordance with the decision to include only electrical effects and not friction losses in those regions, were calculated from

$$\Delta P_{m_1} = \dot{v}\left(p_{-\infty} - p_1\right)_{\substack{\text{power}\\\text{on}}} - \dot{v}\left(p_{-\infty} - p_1\right)_{\substack{\text{power}\\\text{off}}} \tag{44}$$

$$\Delta P_{m_2} = \dot{v}\left(p_2 - p_{\infty}\right)_{\substack{\text{power}\\\text{on}}} - \dot{v}\left(p_2 - p_{\infty}\right)_{\substack{\text{power}\\\text{off}}} \tag{45}$$

The second terms in the above relations were measured in a separate series of runs with zero magnetic field.

The total input power was calculated from

$$P_m = P_{m_0} + \Delta P_{m_1} + \Delta P_{m_2} \tag{46}$$

and the efficiency from

$$\eta = \frac{P_e}{P_m} \tag{47}$$

The measured quantities and the performance values calculated from them are summarized in Table I. The highest output power and efficiency was obtained during Run 6 for which

$$V_1 = 301.2\ \text{ft/sec}$$

$$\dot{m} = 16.42\ \text{lb/sec}$$

$$E = 0.590\ \text{v}$$

$$B_0 = 5.69\ \text{kilogauss}$$

$$\mu = 0.769$$

$$I_L = 18,250\ \text{amp}$$

$$P_e = 10.76\ \text{kw}$$

$$P_{m_0} = 20.85\ \text{kw}$$

$$P_m = 22.40\ \text{kw}$$

$$\eta = 48.1\%$$

The output power P_e is accurate within ±1%, but P_m and η could be in error by as much as 3% because of the 0.7% turbine meter uncertainty which enters into the V_1^3 term in Eq. 43.

Comparison With Theory

The theoretical field, input power, and efficiency were calculated for the conditions of each of the six runs using Eqs. 30, 38, and 39, respectively. For the theoretical calculations the pressure drop was taken as zero and a constant loading ratio $\mu = 0.77$ was used as representing the mean of the experimental values, which ranged from

0.760 to 0.778. The theoretical calculations are summarized in Table II.

Required Field

Figure 8 presents the effect of inlet velocity on the values of magnetic field theoretically and experimentally required for zero pressure drop. Both the theoretical and actual values increase approximately with the square root of the inlet velocity, but the actual field required was 5 to 15% higher than the theoretical. One explanation is that there may have been a contact resistance that raised the NaK voltage above the electrode voltage. A resistance equivalent to 0.15 in. of NaK, for example, would have raised the loading ratio on the NaK side from 0.77 to 0.81, increasing the theoretical field requirement by 10% (and also increasing the generator efficiency, evaluated on the NaK side, by 5%). It is evident that a direct measurement of the liquid potential should be made in tests such as these.

Input Power

Figure 9 presents the theoretical and experimental power inputs at the ends, ΔP_{m1} and ΔP_{m2}, and their sum ΔP_m, as a function of the inlet velocity. The theoretical values were calculated from Eq. 32. It is seen that there is substantial disagreement. The experimental upstream power was negative (that is, the liquid was being pumped), since there was a decrease in upstream pressure drop, $p_{-\infty} - p_1$, when power was generated. During Run 6, for example, the upstream pressure drop was 77 psi, whereas the pressure drop at the same flow rate with zero field was 86 psi.

The experimental downstream power was positive, but eight times larger than the theoretical value. The sum of the experimental upstream and downstream powers agreed better with the theoretical values, being twice the latter.

A possible explanation for the observed behavior is that there was incomplete compensation of the induced field, resulting in the familiar reduction in power generation upstream and increase downstream. The induced field could be appreciable, since the magnetic Reynolds number $\mu_0 \sigma b V_1$ reached 2.3 in the tests.

Pressure Profile

Figure 10 compares the measured and theoretical pressure variation, relative to the inlet pressure, within the diverging channel for Run 6. The theoretical variation was calculated by solving Eq. 30 for Δp and replacing L by x.

It is seen that the actual pressure rose 30% more than the theoretical and peaked farther downstream. This could, again, reflect incomplete induced-field compensation with excess kinetic power available for pressure recovery at the upstream end, followed by a steeper pressure drop as the excess power is extracted at the downstream end.

Efficiency

Figure 11 compares the theoretical and experimental variation of efficiency with inlet velocity. The efficiency increases slowly with velocity because of the increasing Reynolds number and decreasing C_f. The theoretical efficiencies vary from 56.0% at V_1 = 140 ft/sec to 57.7% at V_1 = 301 ft/sec, while the measured efficiencies range from 40.6% to 48.1%. The ratio of measured to theoretical efficiency varies from 0.72 to 0.83.

The measured efficiencies are about 4 percentage points lower than the preliminary values reported earlier[1, 7] because of data-reduction corrections and the introduction of the profile factor 128/245 in place of 1/2 in calculating kinetic power.

The deviation between experimental and theoretical efficiency could be due, in part, to the contact-resistance and induced-field effects suggested earlier. It could also be due to an increase in skin-friction coefficient over the pipe-flow value. An increase in C_f from 0.00306 to 0.0055 would, by itself, bring the theoretical efficiency for Run 6 down to the experimental value.

Output Power

Figure 12 compares the theoretical and experimental output powers. The experimental values range from 75 to 86% of theoretical.

Ultimate Performance Capability

The reasonably close approach of the experimental performance to the theoretical makes it of interest to examine the ultimate performance predicted by the theory.

The basic limitation on the efficiency is the fluid friction, which requires the generator to be short with resulting large end losses. With an exponential field extension, however, the end losses in short generators can be made acceptable.

Figure 13 presents the variation of efficiency with length aspect ratio L/a_m, with and without field extension, for a generator of cross section aspect ratio a_m/b = 3 and velocity ratio V_1/V_2 = 2 at various values of skin-friction coefficient C_f. The field extension assumed is x_e = 3b, a value readily obtainable and approximately that of the experimental generator. It is seen that the influence of fluid friction is greatly reduced with the field extension as compared with sharp cutoff, since the optimum length is reduced.

When the optimum length is employed, the limiting efficiency (for the chosen geometry) reduces simply to a function of the skin-friction coefficient C_f, and this relationship is shown in Fig. 14. The effect of field extension is to decrease the slope of performance loss with friction. For the geometry considered, the limiting efficiency at C_f = 0.003, corresponding to a generator of about 10 kw output, is 64%. For C_f = 0.0013, corresponding roughly to an output of 100 Mw, the efficiency is 68%.

Acknowledgments

The analysis and design of the experimental generator, and the design of the NaK facility, were supervised by C. A. McNary, and the construction of the facility was supervised by T. R. Atkinson and W. A. Stratton. The generator was assembled and installed by A. G. Nelson and D. O'Connor.

H. Otte performed the magnet calibration and pole shaping. The facility checkout and generator tests were supervised by D. J. Cerini, assisted by D. O'Connor. E. Weinberg determined the NaK properties, and A. Otte assisted in the data reduction and analysis.

References

1. Elliott, D. G., Cerini, D. J., and Weinberg, E., Investigation of Liquid MHD Power Conversion, AIAA Paper No. 64-760. Third Biennial Aerospace Power Systems Conference. Philadelphia, Pa., September 1-4, 1964.

2. Brouillette, E. C., and Lykoudis, P. S., "Measurements of Skin Friction for Turbulent Magnetofluidmechanic Channel Flow," Proceedings of the Fourth Symposium on the Engineering Aspects of Magnetohydrodynamics, University of California, Berkeley, April 10-11, 1963.

3. Eckert, E. R. G., Heat and Mass Transfer, 2nd Edition, McGraw-Hill, New York, 1959, p. 156.

4. Sutton, G. W., Hurwitz, H., Jr., and Poritsky, H., "Electrical and Pressure Losses in a Magnetohydrodynamic Channel Due to End Current Loops," AIEE Transactions, Vol. 58, No. 1, pp. 687-695, January 1962.

5. Jackson, C. B. (Editor in Chief), Liquid Metals Handbook, Sodium-NaK Supplement, Third Edition, Atomic Energy Commission, Department of the Navy, Washington, D. C., July 1955, p. 39.

6. Elliott, D. G., Cerini, D. J., and O'Connor, D., "Liquid MHD Power Conversion," Space Programs Summary No. 37-26, Vol. IV, pp. 124-131, Jet Propulsion Laboratory, Pasadena, California, April 30, 1964.

7. Elliott, D. G., Cerini, D. J., Hays, L., O'Connor, D., and Weinberg, E., "Liquid MHD Power Conversion," Space Programs Summary No. 37-28, Vol. IV, pp. 86-92, Jet Propulsion Laboratory, Pasadena, California, August 31, 1964.

Table I. Measured Performance of Experimental Generator

Run No.	$\dot{m}$ lb/sec	V_1 ft/sec	B_0 kilogauss	E v	μ	I_L kiloamp	P_e kw	$p_1 - p_2$ psi	P_{m_0} kw	ΔP_{m_1} kw	ΔP_{m_2} kw	ΔP_m kw	P_m kw	η
1	7.67	140.7	3.51	0.168	0.761	5.48	0.921	1.0	2.15	-0.11	0.23	0.12	2.27	0.406
2	10.10	185.3	4.18	0.263	0.760	8.54	2.248	3.1	4.96	-0.25	0.50	0.25	5.21	0.431
3	12.02	220.5	4.69	0.353	0.763	11.36	4.010	2.5	8.29	-0.29	0.84	0.55	8.84	0.454
4	13.58	249.2	5.05	0.432	0.767	13.69	5.911	1.7	11.89	-0.34	1.31	0.97	12.86	0.459
5	15.05	276.1	5.32	0.512	0.778	15.95	8.158	-1.6	15.98	-0.43	1.69	1.26	17.24	0.473
6	16.42	301.2	5.69	0.590	0.769	18.25	10.764	0.0	20.85	-0.56	2.11	1.55	22.40	0.481

Table II. Theoretical Performance of Experimental Generator at μ = 0.77 and Δp = 0

V_1 ft/sec	Re	C_f	B_0 kilogauss	P_{m_0} kw	ΔP_{m_1} kw	ΔP_{m_2} kw	ΔP_m kw	P_m kw	η	P_e kw
140.7	3.49×10^5	3.50×10^{-3}	3.34	2.124	0.045	0.026	0.071	2.195	0.5600	1.229
185.3	4.59	3.33	3.86	4.852	0.105	0.059	0.164	5.016	0.5666	2.842
220.5	5.47	3.23	4.22	8.184	0.178	0.100	0.278	8.462	0.5706	4.828
249.2	6.18	3.18	4.50	11.812	0.258	0.145	0.403	12.215	0.5714	6.980
276.1	6.84	3.10	4.75	16.060	0.352	0.199	0.551	16.611	0.5756	9.561
301.2	7.46	3.06	4.96	20.851	0.458	0.259	0.717	21.568	0.5772	12.449

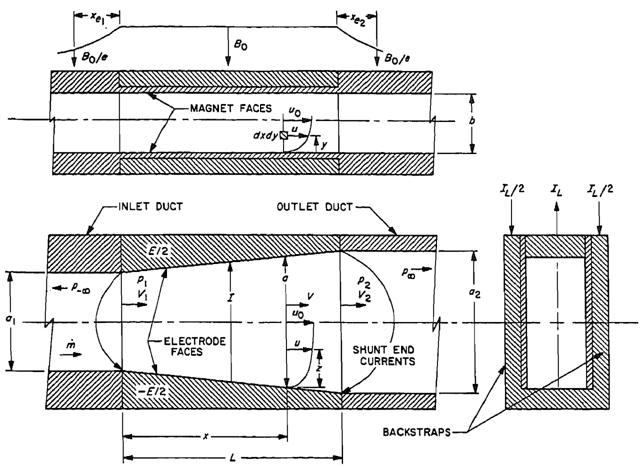

Fig. 1. IDEALIZED MHD GENERATOR

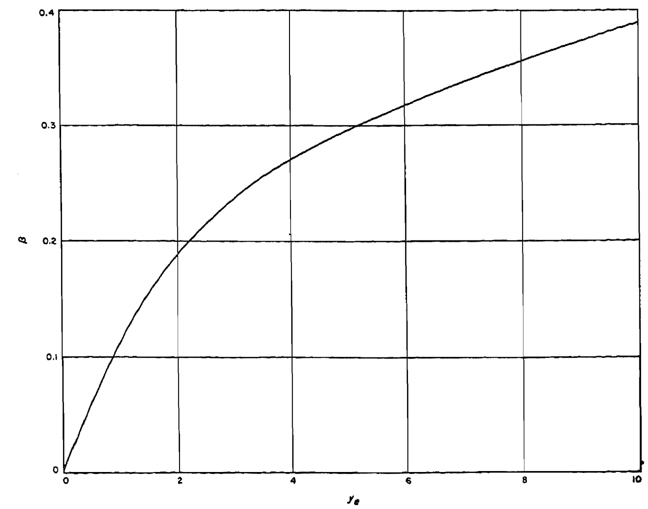

Fig. 2. VARIATION OF INPUT POWER FACTOR β WITH FIELD EXTENSION RATIO y_e (FROM REF. 4)

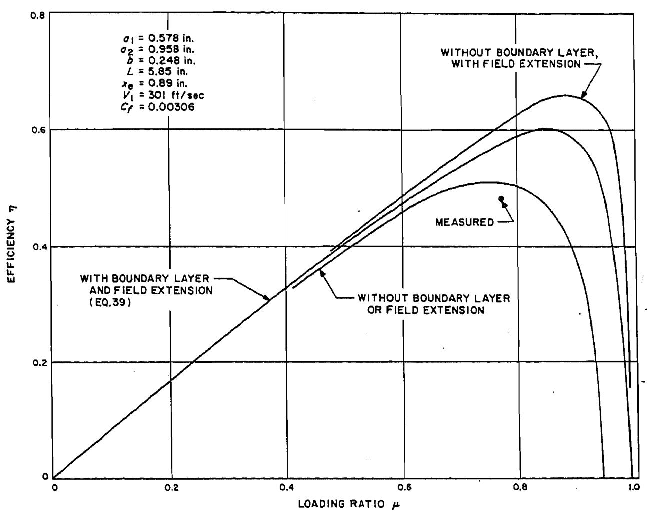

Fig. 3. THEORETICAL EFFICIENCY, WITH AND WITHOUT BOUNDARY LAYER AND FIELD EXTENSION, OF EXPERIMENTAL GENERATOR AT CONDITIONS OF RUN 6

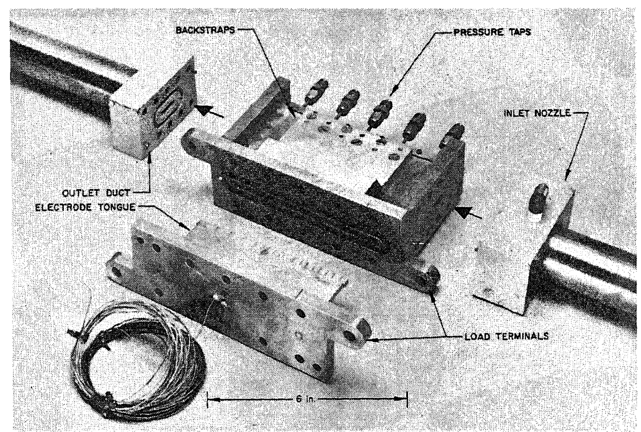

Fig. 4. EXPERIMENTAL GENERATOR

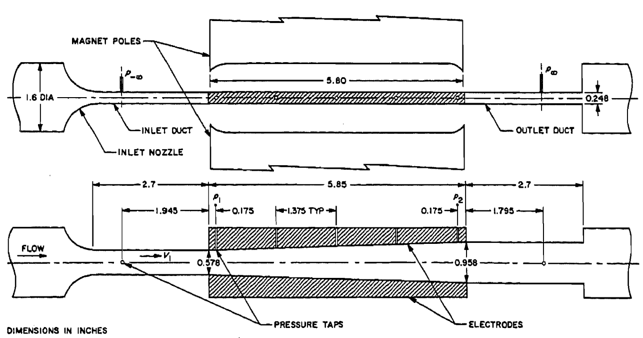

Fig. 5. GEOMETRY OF EXPERIMENTAL GENERATOR

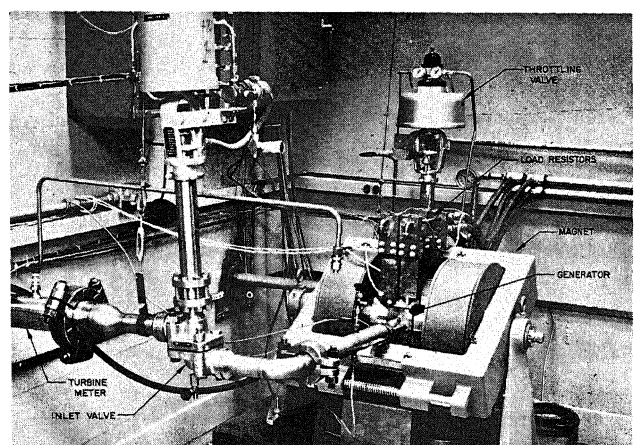

Fig. 6. GENERATOR TEST INSTALLATION

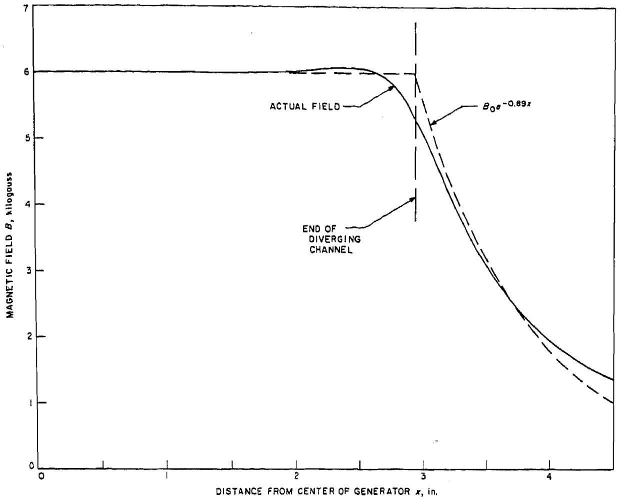

Fig. 7. MAGNETIC FIELD ALONG GENERATOR CENTER LINE, COMPARED WITH EXPONENTIAL FIT

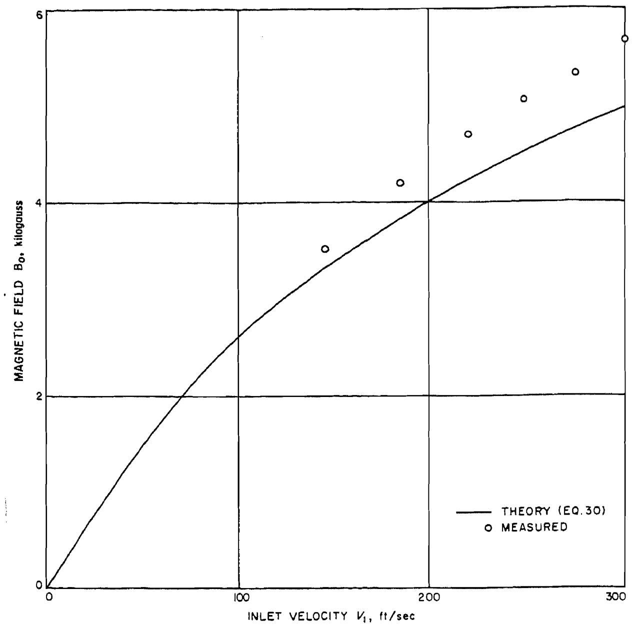

Fig. 8. COMPARISON OF EXPERIMENTAL AND THEORETICAL FIELDS REQUIRED FOR ZERO PRESSURE DROP

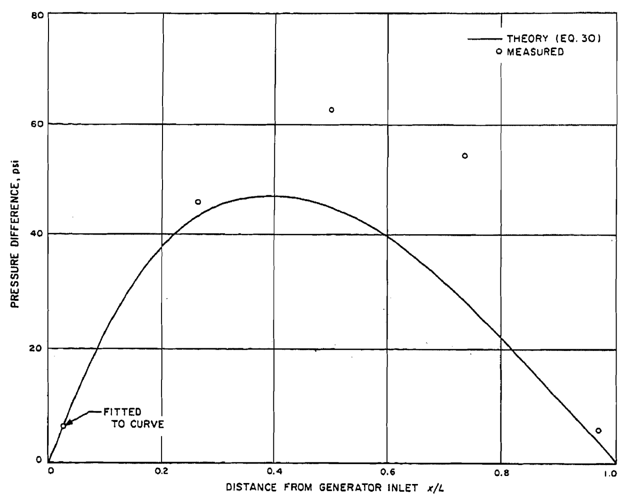

Fig. 10. COMPARISON OF THEORETICAL AND EXPERIMENTAL PRESSURE PROFILES FOR RUN 6

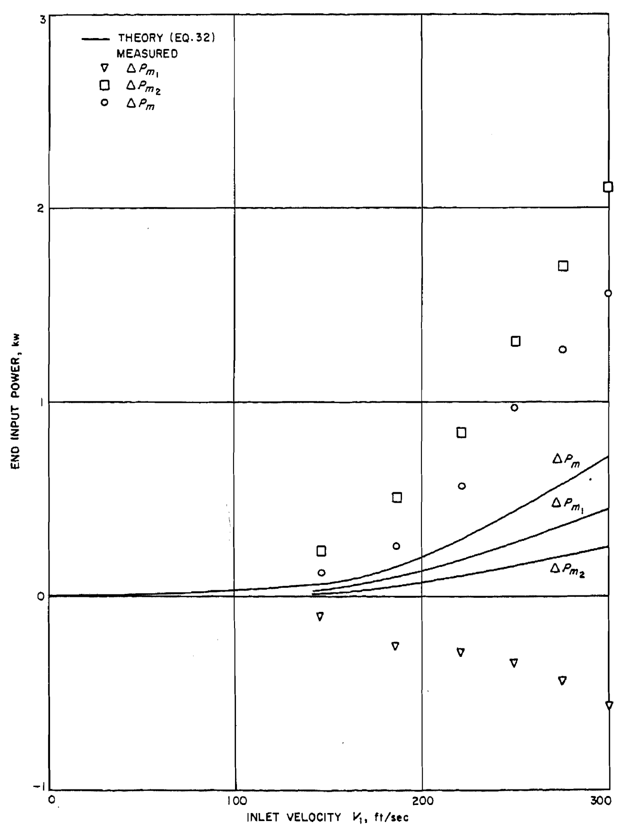

Fig. 9. COMPARISON OF EXPERIMENTAL AND THEORETICAL END INPUT POWERS

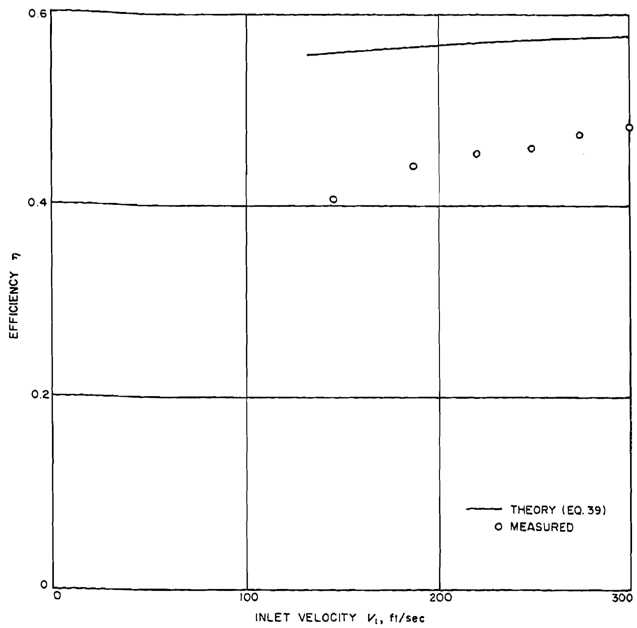

Fig. 11. COMPARISON OF EXPERIMENTAL AND THEORETICAL EFFICIENCIES

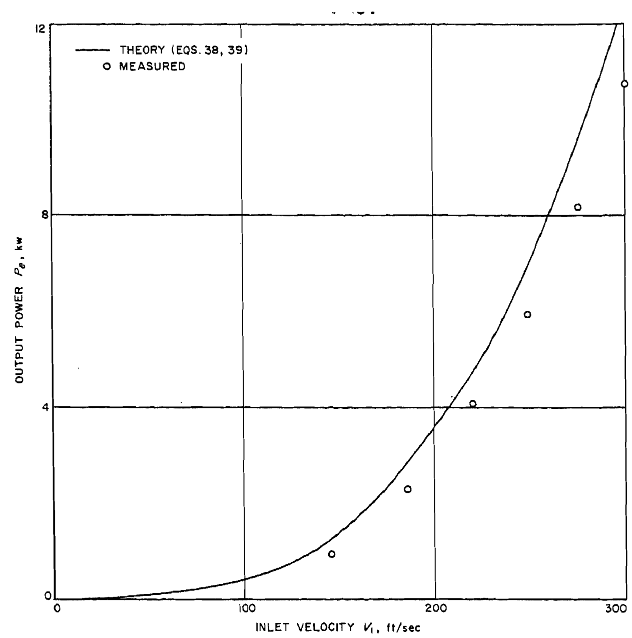

Fig. 12. COMPARISON OF EXPERIMENTAL AND THEORETICAL OUTPUT POWERS

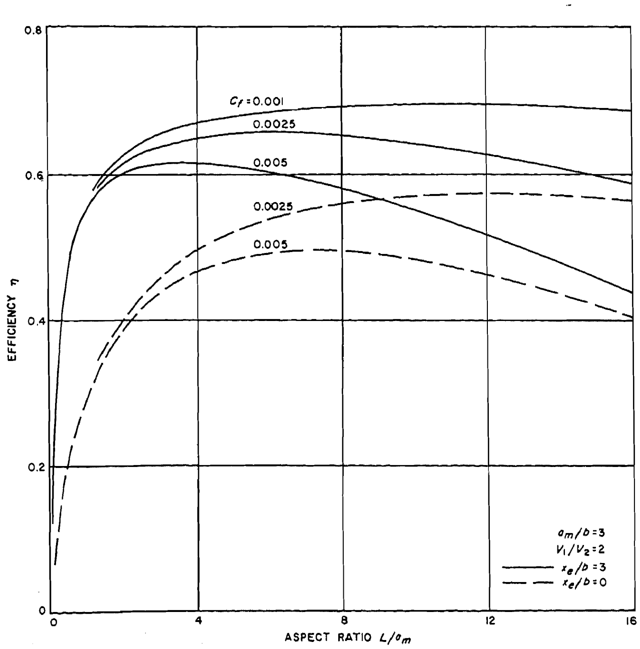

Fig. 13. EFFECT OF ASPECT RATIO ON EFFICIENCY, WITH AND WITHOUT FIELD EXTENSION, AT OPTIMUM LOADING RATIO (DOTTED CURVES ALSO IGNORE BOUNDARY LAYER)

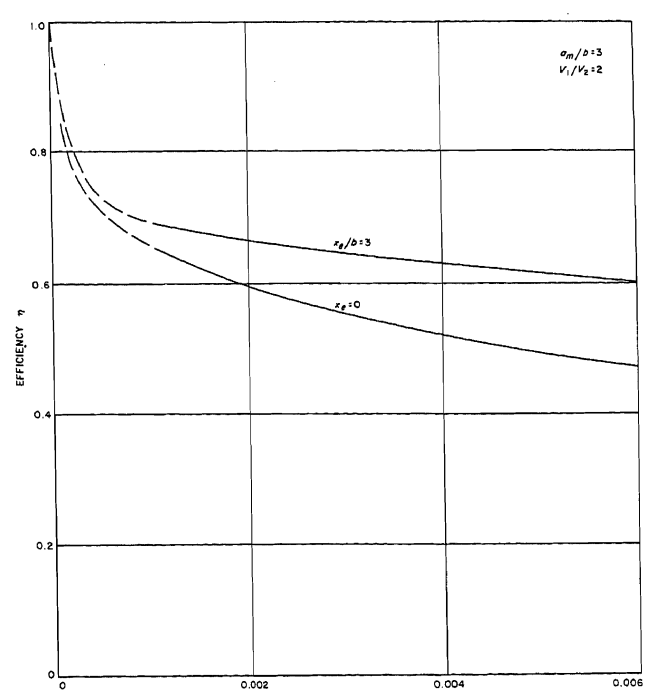

Fig. 14. EFFECT OF SKIN-FRICTION COEFFICIENT ON EFFICIENCY AT OPTIMUM LOADING AND LENGTH